ACS APPLIED MATERIALS & INTERFACES

www.acsami.org

Research Article

Dual-Modal Photon Upconverting and Downshifting Emissions from Ultra-stable $CsPbBr_3$ Perovskite Nanocrystals Triggered by Co-Growth of Tm:$NaYbF_4$ Nanocrystals in Glass

Xiaoyan Li, Changbin Yang, Yunlong Yu, Zheng Li, Jidong Lin, Xiangfeng Guan, Zhiqiang Zheng,* and Daqin Chen*

Cite This: *ACS Appl. Mater. Interfaces* 2020, 12, 18705−18714

Read Online

ACCESS | Metrics & More | Article Recommendations | Supporting Information

ABSTRACT: This work reports a novel dual-phase glass containing Tm:$NaYbF_4$ upconverting nanocrystals (UCNCs) and $CsPbBr_3$ perovskite nanocrystals (PNCs). The advantages of this kind of nanocomposite are that it provides a solid inorganic glass host for the in situ co-growth of UCNCs and PNCs, and protects PNCs against decomposition affected by the external environment. Tm:$NaYbF_4$ NC-sensitized stable $CsPbBr_3$ PNCs photon UC emission in PNCs is achieved under the irradiation of a 980 nm near-infrared (NIR) laser, and the mechanism is evidenced to be radiative energy transfer (ET) from Tm^{3+}: $^1G_4$ state to PNCs rather than nonradiative Förster resonance ET. Consequently, the decay lifetime of exciton recombination is remarkably lengthened from intrinsic nanoseconds to milliseconds since carriers in PNCs are fed from the long-lifetime Tm^{3+} intermediate state. Under the simultaneous excitation of the ultraviolet (UV) light and NIR laser, dual-modal photon UC and downshifting (DS) emissions from ultra-stable $CsPbBr_3$ PNCs in the glass are observed, and the combined UC/DS emitting color can be easily altered by modifying the pumping light power. In addition, UC exciton recombination and Tm^{3+} 4f−4f transitions are found to be highly temperature sensitive. All these unique emissive features enable the practical applications of the developed dual-phase glass in advanced anti-counterfeit and accurate temperature detection.

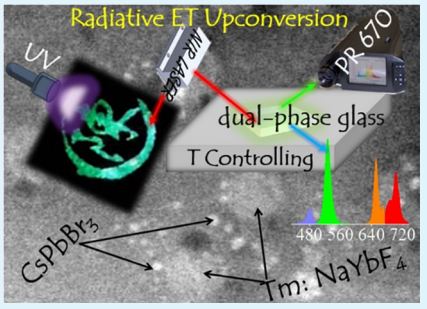

KEYWORDS: *perovskite quantum dots, $CsPbBr_3$, lanthanide ions, $NaYbF_4$, luminescent glasses*

1. INTRODUCTION

All-inorganic cesium lead halide ($CsPbX_3$, X = Cl, Br, and I) perovskite nanocrystals (PNCs) or quantum dots have been extensively investigated in recent years.[1−7] Benefited from their superior optical performance, such as narrow full width at half maxima (FWHM), precisely tunable bandgap, large absorption cross-section, and high photoluminescence quantum yield (PLQY), PNCs have been explored for promising applications in lighting, display, and lasing.[8−14] However, different from PL or downshifting (DS) emission, nonlinear upconverting (UC) emission in PNCs is difficult to be achieved because of the absence of the intermediate energy level and the low efficiency ($<10^{-8}$) of multiphoton absorption.[15−19] In addition, expensive high-energy pulsed lasers are required to excite PNCs. In contrast, trivalent lanthanide (Ln^{3+})-doped NCs can produce more efficient ($>10^{-3}$) UC emissions via a multistep photon absorption and successive energy transfer (ET) processes with the assistance of multiple intermediate excited states of Ln^{3+} and can thus be efficiently pumped by a low-cost continuous-wave diode laser.[20−23] Unfortunately, there are inherent shortages of wavelength tunability for Ln-doped UCNCs due to the defined and discrete energy states of Ln^{3+} ions. Therefore, it is interesting to combine these two kinds of materials together and investigate their optical interactions to explore new emitting materials.

Recently, UC luminescence in PNCs has been reported by radiative reabsorption from Yb/Tm:$LiYF_4$ NCs instead of a nonradiative Förster resonance energy transfer (FRET) process, where Yb/Tm:$LiYF_4$ UCNCs act as an effective sensitizer of PNCs to improve their UC efficiency.[24] Accordingly, fine color-tunable emissions with wavelengths beyond the availability of Ln^{3+} are realized by tuning bandgaps of PNCs under the excitation of a low-power laser diode. Unfortunately, the experimental scheme was achieved by mechanically mixing UCNCs with PNCs in a solution, and PNCs suffered from instability with the prolongation of the storage time due to their ionic crystal feature and low formation energy. Therefore, it is highly desirable to explore a new route to solve this intrinsic drawback.

Received: February 1, 2020
Accepted: March 27, 2020
Published: March 27, 2020

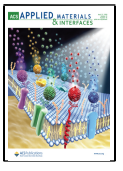

https://dx.doi.org/10.1021/acsami.0c01968
ACS Appl. Mater. Interfaces 2020, 12, 18705−18714

In the present work, Tm:$NaYbF_4$ and $CsPbBr_3$ dual-phase nanoparticles were simultaneously precipitated inside the same glass via an in situ melt-quenching and subsequent glass crystallization technique. Among several strategies to improve the stability of PNCs, it has been proved that the method to incorporate PNCs into a robust inorganic oxide glass can really solve the issue of poor long-term stability of PNCs.[25−30] As far as we know, there is still no report concerning the simultaneous growth of UCNCs and PNCs in the dual-phase glass and their relevant optical interactions in this kind of nanocomposite. As schematically illustrated in Figure 1, in situ

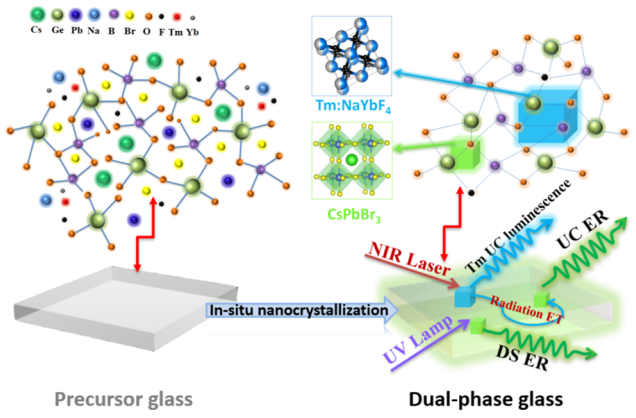

Figure 1. Schematic illustration of the in situ crystallization process of Tm:$NaYbF_4$ UCNC and $CsPbBr_3$ PNC dual-phases inside a germanium borate glass via heat treatment, the relevant glass network of nanocomposites, crystal structures of $NaYbF_4$ and $CsPbBr_3$, and dual-modal excitable UC/DS exciton recombination (ER). Tm^{3+} UC luminescence in $NaYbF_4$ NCs is excited by the NIR laser, and UC ER of $CsPbBr_3$ PNCs is realized via radiative energy transfer (ET) from Tm^{3+} to PNCs. The routine DS ER of $CsPbBr_3$ PNCs is produced upon the irradiation of a UV lamp.

precipitation of both Tm:$NaYbF_4$ NCs and $CsPbBr_3$ PNCs via heating the well-designed Ge−B−Zn−Ca−Na−Cs−Pb−Yb−Tm-based oxyhalide glass can induce efficient radiative ET UC emissions from Tm:$NaYbF_4$ NCs to $CsPbBr_3$ PNCs upon near-infrared (NIR, 980 nm) laser excitation and can produce dual-modal UC/DS emissions of PNCs when excited by both ultraviolet (UV) lamp and NIR laser. Impressively, the combined UC/DS emissive color can be remarkably altered by changing the pumping light power, and the UC emissions from exciton recombination and Tm^{3+} 4f−4f transitions are highly temperature sensitive, enabling their practical applications in anti-counterfeiting and temperature sensing.

2. EXPERIMENTAL SECTION

The dual-phase glasses containing $NaYbF_4$ NCs and $CsPbBr_3$ PNCs were prepared by a traditional melt-quenching and subsequent heating technique. Herein, Ge−B−Zn−Ca−Na−Cs−Pb−Yb−Tm-based oxyhalide glass with various glass compositions were designed, as tabulated in Table S1.

All the raw materials were manually mixed and ground into powders in the mortar for about 60 min. The obtained mixed powders were dissolved in a crucible at 1000 °C for 30 min under an ambient atmosphere. Then the resulting melt was poured into a preheated copper mold and pressed to form a plate of ∼2 mm thickness to obtain a precursor glass (PG), and all the obtained glasses were of the same dimensions all the time. Finally, the dual-phase embedded glass was successfully prepared through controllable in situ glass crystallization via heating at 500 °C for 10 h. Also, the glass containing only Tm^{3+}:$NaYbF_4$ UCNCs was prepared via a similar procedure.

To identify the crystallization phase, X-ray diffraction (XRD) analysis was carried out with a powder diffractometer (MiniFlex600 Rigaku) using Cu Kα radiation (λ = 0.154 nm). The microstructure of the sample was studied by a transmission electron microscope (TEM) (JEM-2010) operated at 200 kV. Scanning TEM (STEM) image was obtained using an FEI aberration-corrected Titan Cubed S-Twin transmission electron microscope operated in a high-angle annular dark-field (HAADF) mode. The absorption spectrum was measured by a UV−vis spectrophotometer (UV-2600, Shimadzu) in a transmittance mode. PL, PL excitation (PLE), and UC emission spectra for the dual-phase glass samples were recorded on an Edinburgh Instrument (EI) FLS1000 spectrofluorometer equipped with continuous (450 W) xenon lamps and a 980 nm laser diode. PLQYs, defined as ratio of the emitted photons to absorbed ones, were determined by combining a 15 cm integrated sphere with an FLS1000 spectrofluorometer. Time-resolved PL traces for exciton recombination were detected on a fluorescent lifetime spectrometer (EI, LifeSpec-II) based on a time-correlated single-photon counting technique under the excitation of a 375 nm picosecond laser. UC decay curves were recorded with a customized UV to mid-infrared steady-state and phosphorescence lifetime spectrometer (FSP920-C, Edinburgh). Temperature-dependent UC emission spectra were recorded on a Fluorolog 3−22 spectrofluorometer (Horiba JY Instruments) with an R928P photomultiplier for signal detection and a temperature controlling stage (THMS600). Notably, the as-synthesized PNC-embedded glasses (i.e., glass plates) were used for optical measurements.

Security inks were made by mixing the ground dual-phase glass powders with commercial blank screen-printing ink (SND-100, purchased from ZHONGYI INK & PAINT CO., LTD, China). Using the above luminescent inks, a series of designed patterns were printed on a black metal plate. UC/DS luminescence images were recorded by a camera (Canon, EOS 80D, EF-S 18−200 mm f/3.5−5.6 IS) in an all-manual mode using an NIR laser and UV lamp as excitation sources.

3. RESULTS AND DISCUSSION

An elaborate design of the glass composition and network structure is an essential prerequisite for the in situ nucleation/growth of the specific crystals inside the glass. Herein, PGs with mole compositions (mol %) of $50GeO_2$-$20B_2O_3$-5ZnO-3CaO-$6Na_2O$-xPbO-yCsBr-$z$$YbF_3-0.1TmF_3$ (x = 0−7 mol %, y = 8−20 mol %, z = 3−8 mol %, Table S1) were optimized to uncover the influence of compositions on glass crystallization. Notably, the boro-germanate glass has the advantages such as low melting temperature, excellent chemical durability, and thermal stability, and moderate solubility of halides, making it suitable to precipitate PNCs inside the glass through thermal treatment and providing a stable host to protect PNCs. To identify the crystallized phase, XRD measurement was performed on products with different contents of YbF_3 ($z$$YbF_3$, z = 3, 5, 8, mol %) after heat treatment at 500 °C for 20 h, as shown in Figure 2a. Indeed, XRD patterns evidenced the simultaneous precipitation of the cubic $CsPbBr_3$ phase (JCPDS No. 54-0752) and cubic $NaYbF_4$ phase (JCPDS No. 27-0813) inside the glass. With an increase of the YbF_3 content, diffraction peaks of both $NaYbF_4$ and $CsPbBr_3$ phases significantly enhanced, indicating that high-content YbF_3 in the glass is beneficial for the growth of $NaYbF_4$ and $CsPbBr_3$ NCs. This result is consistent with the previously reported case, where the introduced fluoride compound broke the tight glass network and promoted the nucleation/growth of PNCs in the glass.[31] However, with the increase of the PbO or CsBr content, the growth of the $NaYbF_4$ phase in the glass was

https://dx.doi.org/10.1021/acsami.0c01968
ACS Appl. Mater. Interfaces 2020, 12, 18705−18714

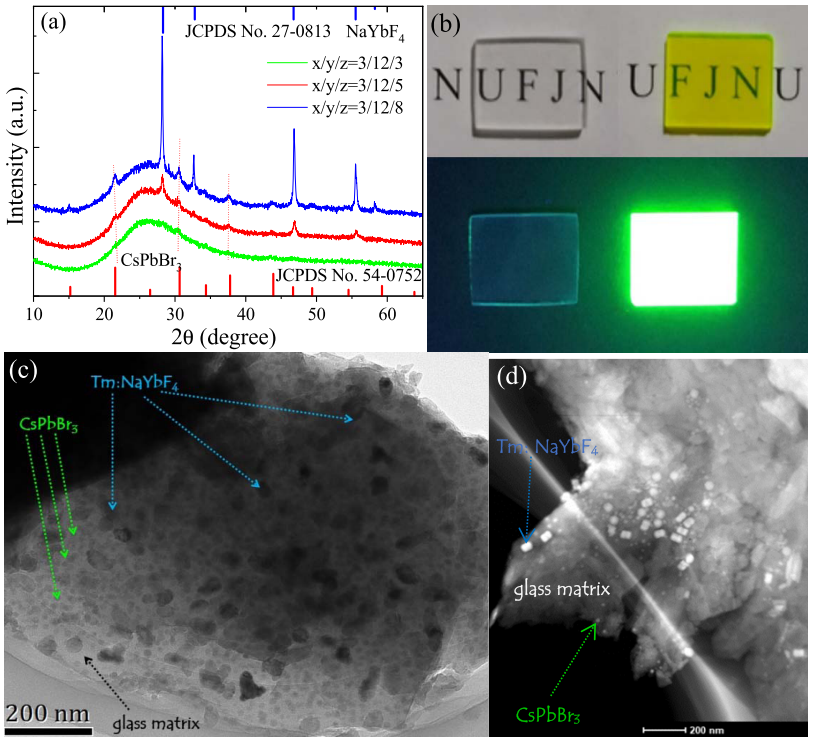

Figure 2. (a) XRD patterns of the dual-phase glass samples with different contents of the YbF_3 component in the glasses. Bars represent the standard diffraction peaks of cubic $NaYbF_4$ (JCPDS No. 27-0813) and cubic $CsPbBr_3$ (JCPDS No. 54-0752) crystals. (b) Photographs of the PG (left) and dual-phase glass (right) under the irradiation of a daylight (top) and UV lamp (bottom). (c) TEM image and (d) HAADF-STEM micrograph of a typical $CsPbBr_3$ and $NaYbF_4$ dual-phase glass.

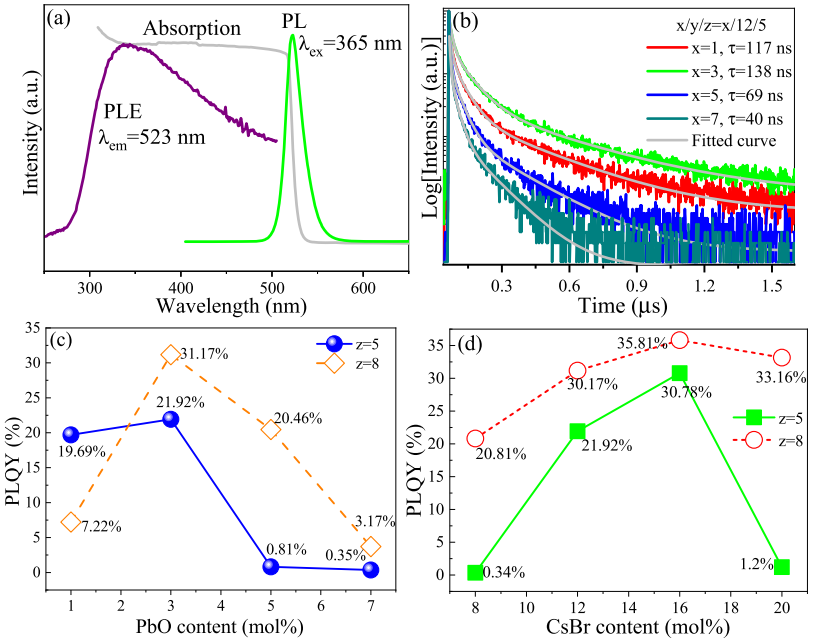

Figure 3. (a) Absorption, PL (λ_{ex} = 365 nm), and PLE (λ_{em} = 523 nm) spectra for a typical $NaYbF_4$ NC and $CsPbBr_3$ PNC dual-phase glass. (b) Time-resolved PL traces (monitoring 523 nm exciton recombination) for the dual-phase glasses with different PbO contents (fixed 12 mol % CsBr and 5 mol % YbF_3) under the excitation of a 375 nm picosecond laser. The multiexponential fitted curves and the average decay lifetimes are shown in the figure. PLQY values for the dual-phase glass samples with (c) various PbO contents (fixed 12 mol % CsBr; 5 or 8 mol % YbF_3) and (d) different CsBr contents (fixed 3 mol % PbO; 5 or 8 mol % YbF_3).

suppressed (Figure S1). These results indicate that glass compositions have a significant impact on the growth of $NaYbF_4$ and $CsPbBr_3$ dual-phase in the glass, and the optimal glass compositions should have the appropriate YbF_3 content (5−8 mol %), PbO content (3−5 mol %), and CsBr content (12−16 mol %). As demonstrated in Figure 2b, the PG is transparent and colorless, and its apparent color is converted into yellow after glass crystallization. Upon the irradiation of a

https://dx.doi.org/10.1021/acsami.0c01968
ACS Appl. Mater. Interfaces 2020, 12, 18705−18714

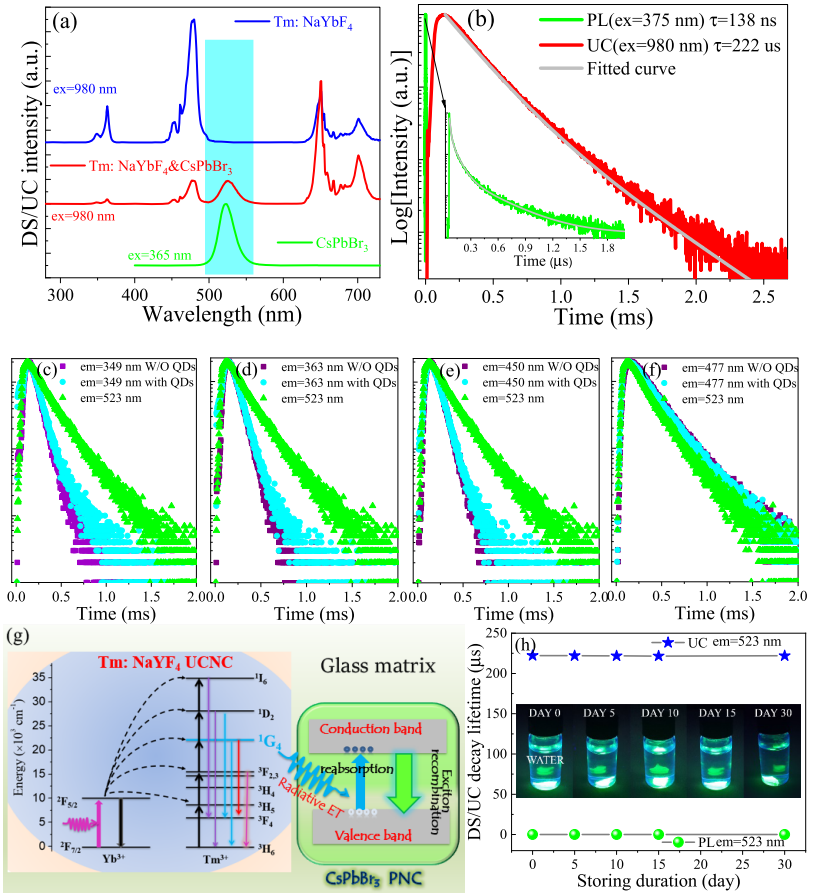

Figure 4. (a) UC emission spectra for the Tm:$NaYbF_4$ single-phase glass and the Tm:$NaYbF_4$ and $CsPbBr_3$ dual-phase glass under 980 nm laser excitation. For comparison, the PL spectrum of exciton recombination in the dual-phase glass excited by 365 nm light is displayed. (b) UC and PL decays of $CsPbBr_3$ PNCs (λ_{em} = 523 nm) in the dual-phase glass sample upon the excitation of a 980 nm pulse laser and 365 nm UV picosecond laser, respectively. The multiexponential fitted curves and the average decay lifetimes are provided. UC decay traces for the dual-phase glass samples with and without (W/O) PNCs by monitoring (c) Tm^{3+} 349 nm ($^1I_6 \rightarrow {}^3F_4$), (d) 363 nm ($^1D_2 \rightarrow {}^3H_6$), (e) 450 nm ($^1D_2 \rightarrow {}^3F_4$), and (f) 477 nm ($^1G_4 \rightarrow {}^3H_6$) emissions. The UC decay curve of 523 nm exciton recombination is added for comparison. (g) Simplified energy-level scheme of the Tm:$NaYbF_4$ and $CsPbBr_3$ dual-phase glass and the proposed radiative energy transfer from Tm^{3+}:$^1G_4$ state to PNCs. (h) Long-term stability test by directly immersing the dual-phase glass in water for 30 days: UC/DS decay lifetimes of exciton recombination versus storing time. Insets are the corresponding luminescent photographs of the dual-phase glass in water.

UV lamp, a bright green DS luminescence was observed. All these results suggest the successful growth of $CsPbBr_3$ PNCs and $NaYbF_4$ NCs in the glass via in situ glass crystallization. Indeed, the TEM image of a typical dual-phase glass (Figure 2c) evidences the homogeneous distribution of $CsPbBr_3$ PNCs with sizes of 5−10 nm and Tm:$NaYbF_4$ NCs with sizes of 30−50 nm in the glass matrix. High-angle annular dark-field scanning TEM (HAADF-STEM) observation, being sensitive to the atomic number (Z) difference in the product, was made to characterize the prepared dual-phase glass. As revealed in Figures 2d and S2, obvious contrast for $CsPbBr_3$ PNCs (small sizes, bright), $NaYbF_4$ NCs (large sizes, bright), and the glass matrix (dark) is distinctly discerned for their large difference in the atomic number among Cs/Pb/Br (Z = 55/82/35), Na/Yb/F (11/70/9), and B/Ge/O (Z = 5/32/8), further verifying the successful precipitation of $CsPbBr_3$ PNCs and $NaYbF_4$ NCs from the GeO_2-based amorphous inorganic glass.

To understand the optical properties of $CsPbBr_3$ PNCs inside the inorganic glass, PL, PLE, and absorption spectra were recorded, as shown in Figure 3a. Under 365 nm excitation, a narrow-band emission peaked at 523 nm with the FWHM of 21 nm was detected. The UV−vis absorption spectrum exhibits a sharp absorption band edge at 518 nm with a relatively smaller Stokes shift of ∼110 cm^{-1}, and the PLE spectrum shows a similar tendency of the band-to-band absorption transition. These results indicate that the luminescence of $CsPbBr_3$ PNCs inside the glass derives from direct exciton recombination, which is consistent with the case of $CsPbBr_3$ colloidal PNCs.[25] Time-resolved decay curves for the dual-phase glasses with different PbO contents (fixed 5 mol % YbF_3 and 12 mol % CsBr) are shown in Figure 3b. Owing to its nonsingle-exponential features, the PL decay of exciton recombination can be well described by three-exponential fitting (Supporting Information), and the fitted parameters are tabulated in Table S2. The evaluated lifetime values are 117, 138, 69, and 40 ns for the PbO content of 1, 3, 5, 7 mol % in the glass, respectively. Figure 3c shows the dependence of the absolute PLQY values on the PbO content, and Figure S3shows the corresponding quantitative PL spectra. Similar to the case of lifetime, PLQY exhibits a maximal value of 21.92% with the PbO content of 3 mol %. When the PbO content is fixed to 3 mol %, it is found that the optimal CsBr content in the glass is 16 mol % and the PLQY value reaches 30.78% (Figures 3d and S4). For the dual-phase glass with 8 mol %

https://dx.doi.org/10.1021/acsami.0c01968
ACS Appl. Mater. Interfaces 2020, 12, 18705−18714

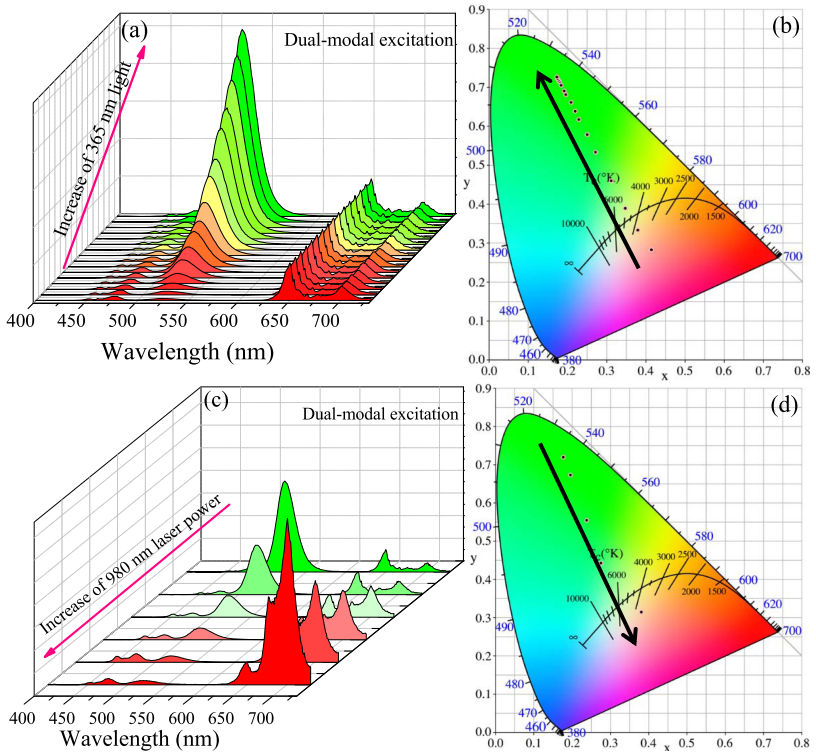

Figure 5. (a, c) UC emission spectra and (b, d) color coordinates in the CIE diagrams for the Tm:$NaYbF_4$ and $CsPbBr_3$ dual-phase glass under the simultaneous excitation of 365 nm UV light and 980 nm NIR laser: (a, b) NIR laser power is fixed and UV light power gradually increases; (c, d) UV light power is fixed and NIR laser power monotonically enhances. The arrows represent an increase of the excitation light power.

YbF_3 content, the same variation tendency can be obtained and the maximal PLQY value is 35.81% for 3 mol % PbO content and 16 mol % CsBr content in the glass (Figures 3c,d, S5 and S6). The improved PLQY of PNCs is believed to be attributed to the promotion of $CsPbBr_3$ growth inside the glass (i.e., high-content PNCs embedded in the glass) with the increase of the YbF_3 content, as evidenced in XRD patterns (Figure 2a). Generally, the detection of Yb^{3+} luminescence at ~980 nm under the excitation of UV light is the direct evidence to confirm the incorporation of Yb^{3+} dopants into $CsPbBr_3$ perovskite NCs.[32,33] However, no Yb^{3+} emission is detected in our samples, indicating that Yb^{3+} ions have not been doped in $CsPbBr_3$ PNCs. This is reasonable since Yb^{3+} ions are difficult to diffuse into the $CsPbBr_3$ lattice in the present dual-phase glass samples due to the hindering role of the glass matrix, which is quite different from the cases of Yb^{3+}-doped colloidal perovskite NCs prepared by the wet chemical method.[32−35]

UC emission spectra for the Tm:$NaYbF_4$ single-phase glass and the Tm:$NaYbF_4$ and $CsPbBr_3$ dual-phase glass were recorded under 980 nm laser excitation (Figure 4a). For the Tm: $NaYbF_4$-embedded glass, typical Tm^{3+} UC emissions were detected and divided into three regions: the UV region with peaks at 349 nm ($^1I_6 \rightarrow {}^3F_4$) and 363 nm ($^1D_2 \rightarrow {}^3H_6$), the blue region with peaks at 450 nm ($^1D_2 \rightarrow {}^3F_4$) and 477 nm ($^1G_4 \rightarrow {}^3H_6$), and the red region with peaks at 650 nm ($^1G_4 \rightarrow {}^3F_4$) and 707 nm ($^2F_{2,3} \rightarrow {}^3H_6$). Importantly, besides Tm^{3+} emissions, an extra UC emitting band at 523 nm was observed for the Tm:$NaYbF_4$ and $CsPbBr_3$ dual-phase embedded glass. This is attributed to the exciton recombination of $CsPbBr_3$ PNCs in the glass by comparing the PL spectra of the dual-phase glass under 365 nm UV light excitation (Figure 4a). As evidenced in Figure S7, the UC emitting intensity of $CsPbBr_3$ PNCs in a series of dual-phase glasses with different glass compositions under 980 nm laser excitation follows the same variation tendency of PLQYs, further confirming that 523 nm band-like UC emission in the present dual-phase glass is indeed originated from $CsPbBr_3$ PNCs. Furthermore, UC (λ_{ex} = 980 nm; λ_{em} = 523 nm) and DS (λ_{ex} = 365 nm; λ_{em} = 523 nm) decay behaviors of $CsPbBr_3$ PNCs in the dual-phase glass sample were investigated, as shown in Figure 4b. It was discovered that the UC decay lifetime of exciton recombination is abnormally much longer than the corresponding DS decay lifetime, which is lengthened from the intrinsic nanosecond scale (138 ns) to milliseconds (222 μs, Table S2).

To reveal the exact UC emission mechanism of $CsPbBr_3$ PNCs in the dual-phase glass, the UC decay curves of the Tm^{3+} $^1I_6 \rightarrow {}^3F_4$, $^1D_2 \rightarrow {}^3H_6$, $^1D_2 \rightarrow {}^3F_4$, and $^1G_4 \rightarrow {}^3H_6$ transitions in the Tm:$NaYbF_4$ single-phase glass and the Tm:$NaYbF_4$ and $CsPbBr_3$ dual-phase glass were recorded under the excitation of a 980 nm pulsed laser (Figure 4c−f). Also, the UC decay curve for the exciton recombination of $CsPbBr_3$ PNCs in the dual-phase glass was recorded. Notably, the UC decay behaviors of Tm^{3+} $^1I_6$, $^1D_2$, and $^1G_4$ emitting states have not been altered after the growth of $CsPbBr_3$ PNCs inside the glass, indicating that the nonradiative FRET from Tm^{3+} in $NaYbF_4$ NCs to $CsPbBr_3$ PNCs does not occur in the present dual-phase glass. Impressively, it was found that the UC lifetime of exciton recombination (523 nm) was very approximate to that of the Tm^{3+} $^1G_4 \rightarrow {}^3H_6$ (477 nm) transition for all the investigated dual-phase glass samples (Figures 4f and S8). More importantly, as shown in Figure S9, the UC decays of the Tm^{3+} $^1G_4$ emitting state in the samples with different CsBr contents (i.e., different amounts of $CsPbBr_3$ PNCs) are almost identical, further verifying that there is no extra electron relaxation channel from the Tm^{3+} $^1G_4$

https://dx.doi.org/10.1021/acsami.0c01968
ACS Appl. Mater. Interfaces 2020, 12, 18705−18714

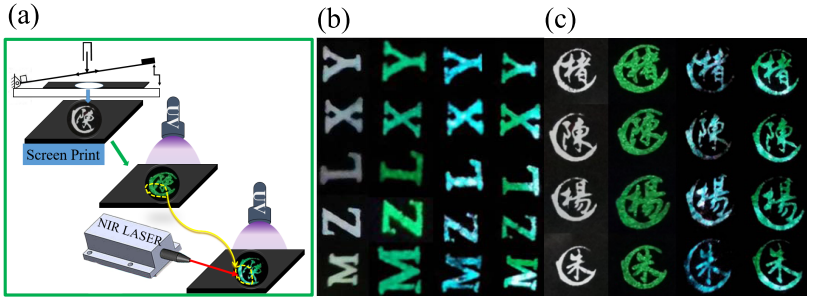

Figure 6. (a) Schematic illustration of the preparation of the anti-counterfeiting pattern via a screen-printing technique and a single-modal or dual-modal excitation strategy. Several anti-counterfeiting luminescent patterns of (b) English letters and (c) Chinese characters fabricated from dual-phase glass inks upon different excitation modes (column 1: daylight, column 2: UV light, column 3: NIR laser, column 4: UV light, and NIR laser).

excited state to the conductive band of $CsPbBr_3$ PNCs. Therefore, all these results evidence that Tm:$NaYbF_4$ UCNC to $CsPbBr_3$ PNC ET in the dual-phase glass should be a radiative reabsorption process rather than a nonradiative FRET one. A simplified diagram of the radiative ET process is schematically illustrated in Figure 4g. Under 980 nm NIR laser excitation, successive multiphonon ET UC processes from Yb^{3+} to Tm^{3+} in Tm:$NaYbF_4$ NCs can populate $^1I_6$, $^1D_2$, and $^1G_4$ excited states of Tm^{3+}, from which UV, blue, and red emissions yield. Among these Tm^{3+} UC emissions, the $^1G_4 \rightarrow {}^3H_6$ radiation can be effectively reabsorbed by $CsPbBr_3$ PNCs, which leads to the obvious difference in the relative intensities of 477 and 650 nm Tm^{3+} emissions in Tm:$NaYbF_4$ and the Tm:$NaYbF_4$ and $CsPbBr_3$ spectra (Figure 4a). This radiative ET can efficiently pump carriers from the valence band to the conduction band and create electron−hole pairs (excitons) in $CsPbBr_3$ PNCs, followed by photon emission through exciton recombination. Therefore, it is reasonable that the UC decay lifetime of exciton recombination relative to its intrinsic PL decay is lengthened by 3 orders of magnitude and approaches to that of the Tm^{3+}:$^1G_4$ emitting state because of the slow population of the PNC excited state from the long-lived Tm^{3+} $^1G_4$ excited state during the radiative ET from UCNCs to PNCs.

Furthermore, the stability of the dual-phase glass was investigated by directly immersing it in water for a certain time period. Time-resolved PL/UC traces for the exciton recombination of $CsPbBr_3$ PNCs and the evaluated decay lifetimes show no obvious change (Figures S10a,b, and 4h). Similarly, UC radiative kinetics of Tm^{3+} is not remarkably affected by the elongation of storing time in water (Figure S10c). Evidently, bright luminescence from the dual-phase glass remains after immersing the glass in water for 30 days (inset of Figure 4h) and nearly 100% spectral intensity is retained (Figure S11). Such superior long-term stability for the present dual-phase glass is benefited from the effective protection of PNCs and UCNCs by the solid inorganic oxide glass.

Benefited from the dual-modal emissive feature of $CsPbBr_3$ PNCs in the dual-phase glass, it is feasible to tune the combined DS/UC luminescence over a broad spectral range upon the simultaneous excitation of a 980 nm laser and 365 nm UV light. First, 980 nm laser power is fixed and the power of incident UV excitation light is gradually raised. As shown in Figure 5a, the corresponding Tm^{3+} UC emissions remain unchanged, while the emission of PNCs is significantly enhanced. As evidenced in the Commission International de I'Eclairage (CIE) 1931 chromaticity diagram (Figure 5b), the combined UC/DS color in the dual-phase glass can alter in a broad region from red to green with an increase of the UV excitation light power. Second, the UV excitation light is fixed, and the NIR laser power gradually increases. As exhibited in Figure 5c, Tm^{3+} UC emissions become intensified, while the emission of PNCs monotonically weakens. This high-power laser-induced decrease of PNC emission is observed for all the other dual-phase glass samples under single-modal 980 nm laser excitation (Figures S12 and S13). Accordingly, the combined emitting color can be tuned from green to pink with an increase of 980 nm laser power (Figure 5d). It is well known that high laser power can result in the enhanced Tm^{3+} UC emissions due to the multiphoton absorption process. Notably, the decreased emission of PNCs is believed to be attributed to a high-power laser-induced heating effect since the exciton recombination probability of PNCs significantly decreases with the increase in temperature (Figure S14). The incident 980 nm laser can be efficiently absorbed by Yb^{3+} ions in the present dual-phase glass, and most of them are converted into heat for the low UC emitting efficiency ($\sim 10^{-3}$). Indeed, this laser-induced photothermal effect can significantly enhance $^2F_{2,3} \rightarrow {}^3H_6$ (707 nm) UC emission (Figure 5c) via thermal repopulation between the $^3F_{2,3}$ and $^3H_4$ states of Tm^{3+} (Figure S15).

As a proof-of-concept experiment, we demonstrated the practical application of the dual-phase glass in anti-counterfeiting benefited from DS/UC dual-modal emissions of PNCs excitable by UV lamp and NIR laser. A series of luminescent patterns were designed using the dual-phase glass inks, and the designed patterns were printed on a metal plate via a screen-printing technique. As evidenced in Figure 6, all the patterns (English letters and Chinese characters) show an obvious change of emitting color with the modification of excitation sources. Under the irradiation of a 365 nm UV lamp, the patterns show green luminescence originated from the routine DS emission of $CsPbBr_3$ PNCs. Upon the irradiation of a 980 nm NIR laser, the patterns exhibit cyan luminescence due to the combined UC emissions of Tm^{3+} activators and $CsPbBr_3$ PNCs. Interestingly, dual-color emissions can be detected upon the simultaneous excitation of a UV lamp and NIR laser, where the cyan UC luminescence is superposed on the green DS luminescence via a scanning 980 nm laser on a section of these letters or characters. Notably, the UC efficiency of PNCs upon NIR laser excitation is less than the PL efficiency upon UV light excitation. Therefore, the UC luminescence of the printed ink is more sensitive to the homogeneity of PNCs than photoluminescence. This will lead to some white spots for English letters and Chinese characters upon NIR laser

https://dx.doi.org/10.1021/acsami.0c01968
ACS Appl. Mater. Interfaces 2020, 12, 18705−18714

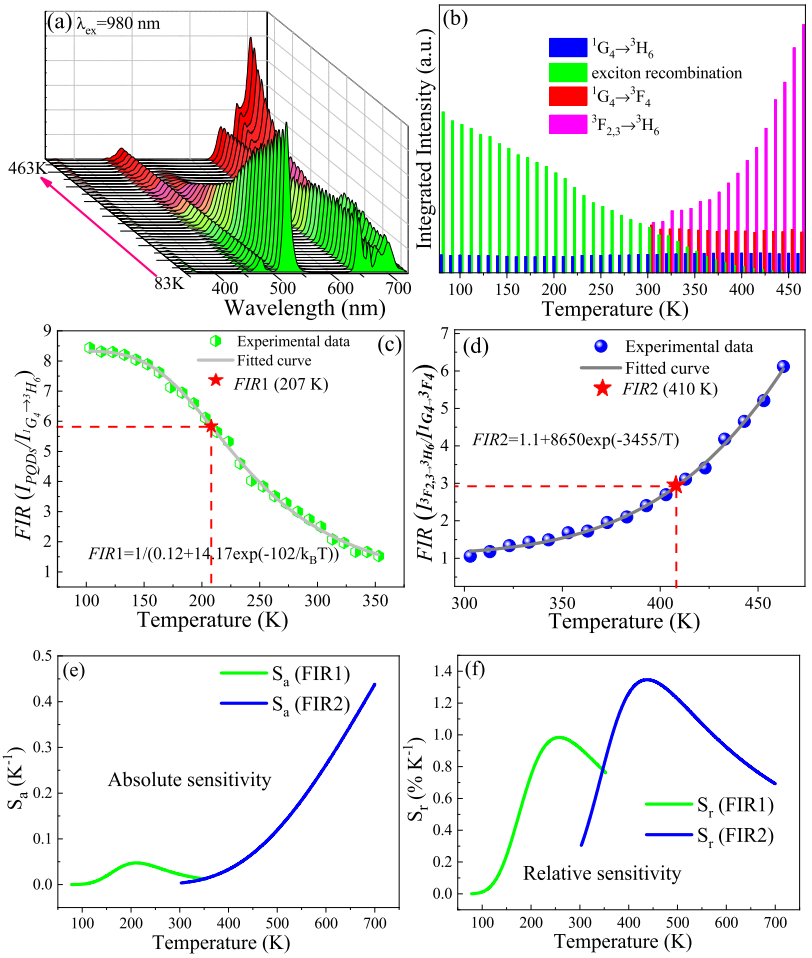

Figure 7. (a) Temperature-sensitive UC emission spectra for the dual-phase glass under 980 nm laser excitation. (b) Temperature-dependent integrated UC intensity of exciton recombination and Tm^{3+} UC emissions at 477 nm ($^1G_4 \rightarrow {}^3H_6$), 650 nm ($^1G_4 \rightarrow {}^3F_4$) and 707 nm ($^2F_{2,3} \rightarrow {}^3H_6$). Measured and fitted plots of (c) fluorescence intensity ratio (FIR) ($I_{PNCs}/I477$ nm) and (d) FIR ($I707$ nm/$I_{650\ nm}$) versus temperature. The fitted curves and the corresponding expressions are provided in the figures. Stars represent the experimentally recorded two FIR values by a spectroradiometer to determine the actual temperature of an object. (e) Absolute sensitivity S_a and (f) relative sensitivity S_r versus temperature.

excitation due to the high PNC content in the corresponding regions. It is worthy to mention that the stability of the ink patterns is excellent owing to the effective protection of perovskite NCs by the glass matrix. Therefore, these versatile dual-modal DS/UC emissive patterns excitable by a cheap and commercial UV lamp and a 980 nm NIR laser are expected to be adopted as flexible anti-counterfeiting labels for security application.

As mentioned above, the present dual-phase glass shows temperature-sensitive UC emissions for both 4f−4f transitions of Tm^{3+} and exciton recombination of PNCs, which may enable it to find a promising application in optical thermometry. Figure 7a shows the related temperature-dependent UC emission spectra under 980 nm laser excitation. Indeed, a remarkable change is found for UC emissions with an increase of temperature. The histograms of the integrated UC intensities for exciton recombination (523 nm) of PNCs, $^1G_4 \rightarrow {}^3H_6$ (477 nm), $^1G_4 \rightarrow {}^3F_4$ (650 nm), and $^2F_{2,3} \rightarrow {}^3H_6$ (707 nm) transitions of Tm^{3+} are presented in Figure 7b. With the elevation of temperature from 83 to 463 K, the UC intensity of $CsPbBr_3$ PNCs significantly decreases owing to temperature-induced nonradiative exciton relaxation, while that of Tm^{3+} emission at 477 nm ($^1G_4 \rightarrow {}^3H_6$) remains almost unchanged. On the other hand, when temperature raises from 300 to 463 K, UC emissions corresponding to Tm^{3+} $^3F_{2,3} \rightarrow {}^3H_6$ and $^1G_4 \rightarrow {}^3F_4$ transitions exhibit opposite temperature-dependent behaviors, i.e., the former remarkably increases while the latter gradually decreases. This is attributed to the competition of the electron population in Tm^{3+} $^3F_{2,3}$ and $^3H_4$ thermally coupled states (TCS).[32] Increasing temperature will populate the upper $^3F_{2,3}$ state from the lower $^3H_4$ state via thermal activation, which will further induce a decrease of electrons in the $^1G_4$ excited state since this state is populated from $^3H_4$ via the energy transfer upconversion (ETU) process (Figure S15).

Accordingly, it is possible to realize temperature detection through experimentally measuring the temperature-sensitive UC fluorescence intensity ratio (FIR) of the dual-phase glass. Importantly, benefited from its multiplex UC emissive feature, we can construct two kinds of FIRs based on 523 nm exciton emission to the Tm^{3+} 477 nm $^1G_4 \rightarrow {}^3H_6$ transition (denoted as FIR1) and Tm^{3+} 707 nm $^3F_{2,3} \rightarrow {}^3H_6$ to Tm^{3+} 650 nm $^1G_4 \rightarrow {}^3F_4$ (denoted as FIR2). Herein, exciton recombination and the Tm^{3+} $^3F_{2,3} \rightarrow {}^3H_6$ transition are temperature-detecting signals for their significant temperature-sensitive emissions, while Tm^{3+}:$^1G_4 \rightarrow {}^3H_6$ and $^1G_4 \rightarrow {}^3F_4$ transitions act as the reference signals for their relatively temperature-insensitive emissions. As shown in Figure 7c,d, FIR1 gradually decreases

https://dx.doi.org/10.1021/acsami.0c01968
ACS Appl. Mater. Interfaces 2020, 12, 18705−18714

and FIR2 increases with the elevation of temperature. The sensor sensitivity is an important parameter in determining the performance of the temperature sensor. Herein, FIR1 can be easily deduced according to the expression of temperature-dependent exciton recombination[7,25]

$$\mathrm{FIR1} = \frac{I_{\mathrm{PNCs\ em}}}{I_{477\ \mathrm{nm}}} \approx \frac{1}{B + C\exp(-\Delta E/k_{\mathrm{B}}T)} \quad (1)$$

where B and C are constants, T is absolute temperature, and k_B is the Boltzmann constant. ΔE is the nominal thermal quenching activation energy for $CsPbBr_3$ PNCs and the Tm^{3+} $^1G_4 \rightarrow {}^3H_6$ dual-emitting system. Indeed, the experimental data can be well fitted with the correlation coefficient above 99.8%, and the obtained ΔE value is 102 meV (Figure 7c), which is close to the exciton binding energy of 125 meV (Figure S14). On the other hand, FIR2 data can be well fitted to the temperature by the following exponential equation[36,37]

$$\mathrm{FIR2} = \frac{I_{707\ \mathrm{nm}}}{I_{650\ \mathrm{nm}}} = D + E \times \exp(-F/T) \quad (2)$$

where D, E, and F are constants, which can be determined by fitting the experimental data (Figure 7d). Therefore, the absolute temperature sensitivity $\left(S_a = \left|\frac{\partial \mathrm{FIR}}{\partial T}\right|\right)$ and the relative sensitivity $\left(S_r = \left|\frac{1}{\mathrm{FIR}}\frac{\partial \mathrm{FIR}}{\partial T}\right|\right)$ can be further derived (Supporting Information) and are plotted in Figure 7e,f for FIR1 and FIR2, respectively. FIR1 shows high sensitivity in the low-temperature region (100−300 K) for the remarkable variation of the UC exciton recombination of PNCs, while FIR2 exhibits high sensitivity in the high-temperature region (300−700 K) since relatively high temperature is required to repopulate $^3F_{2,3}$ and $^3H_4$ TCS (Figure S15). Specifically, the maximal $S_{r(523/477)}$ value reaches 0.98% K^{-1} at 256 K, and the maximal $S_{r(707/650)}$ value is as high as 1.35% K^{-1} at 437 K. Impressively, the temperature sensitivities for the present dual-phase glass are comparable or even superior to the previously reported ones (Table S3).[36,38−42] Therefore, considering the wide operating temperature range and high sensitivity, the strategy based on the emissions from PNCs and Ln^{3+} ion-codoped dual-phase glass is prospective to realize broad/accurate temperature detection. Herein, we designed a real-time temperature-measuring system (Figure 8) consisting of a spectroradiometer (SpectraScan PR670) and a temperature-controlling stage (Linkam THMS600). The temperature can be calibrated by comparing the acquired FIR value with the theoretically calculated FIR curve. As expected, we can accurately determine the temperature by reading out two FIR values at two distinct low/high temperatures and indexing from FIR curves. The values are close to the set temperatures, as illustrated in Figure 7c,d, confirming the feasibility for the proposed temperature-detecting strategy.

4. CONCLUSIONS

In summary, photon UC emission in PNCs excitable by a low-cost NIR laser diode is achieved through the co-growth of $Tm:NaYbF_4$ UCNCs and $CsPbBr_3$ PNCs inside the same glass matrix. This kind of nanocomposite is fabricated via an in situ glass crystallization strategy, and the design and optimization of PG compositions are the necessary prerequisites for the simultaneous precipitation of UCNC and PNC dual-phases in the glass. The UC mechanism in PNCs is evidenced to be $Tm:NaYbF_4$ UCNC-sensitized radiative ET, which is much more efficient than traditional multiphoton absorption and can break the distance limitation on ET efficiency by the random growth of dual-phase nanoparticles in the glass matrix. As a merit of radiative ET UC emissions, the decay lifetimes of excitons fed from the long-lifetime intermediate state of Tm^{3+} have been lengthened by more than 3 orders of magnitude from ~100 ns to ~200 μs. Importantly, the encapsulation of PNCs and UCNCs in the solid glass can solve the issue of long-term stability thoroughly, and almost 100% luminescence of PNCs is retained after directly immersing the product in water for 30 days. These findings offer a general method to produce dual-modal UC and DS emissions from glass-protected ultra-stable PNCs, and the combined luminescence from exciton recombination and Tm^{3+} 4f−4f transitions in the dual-phase glass is highly excitation-source dependent and temperature sensitive, which will bring new prospects for application in the optoelectronic field. As proof-of-concept experiments, we finally demonstrate its practical applications in high-end anti-counterfeiting and real-time temperature sensing.

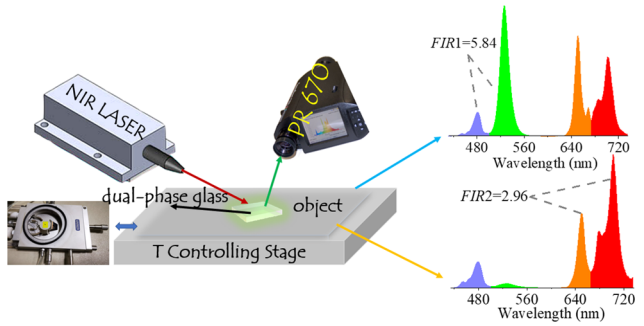

Figure 8. Real-time temperature-measuring system to determine the actual temperature of an object coated with the dual-phase glass. UC emission spectra are directly read out from the emitting region via a spectroradiometer to obtain FIR values. The temperature is precisely controlled through a temperature-controlling stage, and the pumping source is a common 980 nm NIR laser.

■ ASSOCIATED CONTENT

Supporting Information

The Supporting Information is available free of charge at https://pubs.acs.org/doi/10.1021/acsami.0c01968.

Extra XRD, HADDF-STEM image, PL spectra, UC emission spectra, PL decay curves, UC decay curves, and energy level diagram (PDF)

■ AUTHOR INFORMATION

Corresponding Authors

Zhiqiang Zheng − *College of Physics and Energy, Fujian Normal University, Fuzhou 350117, China; Fujian Provincial Collaborative Innovation Center for Advanced High-Field Superconducting Materials and Engineering, Fuzhou 350117, China*; Email: zqzheng@fjnu.edu.cn

Daqin Chen − *College of Physics and Energy, Fujian Normal University, Fuzhou 350117, China; Fujian Provincial Collaborative Innovation Center for Advanced High-Field Superconducting Materials and Engineering, Fuzhou 350117, China; Fujian Provincial Engineering Technology Research Center of Solar Energy Conversion and Energy Storage, Fuzhou*

https://dx.doi.org/10.1021/acsami.0c01968
ACS Appl. Mater. Interfaces 2020, 12, 18705−18714

350117, China; orcid.org/0000-0003-0088-2480; Email: dqchen@fjnu.edu.cn

Authors

Xiaoyan Li − *College of Physics and Energy, Fujian Normal University, Fuzhou 350117, China; College of Electronics and Information Science and Key Laboratory of Green Perovskites Application of Fujian Province Universities, Fujian Jiangxia University, Fuzhou 350108, China; Fujian Provincial Collaborative Innovation Center for Advanced High-Field Superconducting Materials and Engineering, Fuzhou 350117, China*

Changbin Yang − *College of Physics and Energy, Fujian Normal University, Fuzhou 350117, China*

Yunlong Yu − *College of Electronics and Information Science and Key Laboratory of Green Perovskites Application of Fujian Province Universities, Fujian Jiangxia University, Fuzhou 350108, China*

Zheng Li − *College of Physics and Energy, Fujian Normal University, Fuzhou 350117, China*

Jidong Lin − *College of Physics and Energy, Fujian Normal University, Fuzhou 350117, China*

Xiangfeng Guan − *College of Electronics and Information Science, Fujian Jiangxia University, Fuzhou 350108, China*

Complete contact information is available at: https://pubs.acs.org/10.1021/acsami.0c01968

Notes

The authors declare no competing financial interest.

■ ACKNOWLEDGMENTS

This work was supported by the National Natural Science Foundation of China (51972060), the Special Foundation for Theoretical Physics Research Program of China (11847056), the Natural Science Foundation of Fujian Province (2019J01283, 2017J01676, and 2017J01677), and the Training Program for Distinguished Young Scholars in Fujian Province University (Minjiaoke [2017] No. 52).

■ REFERENCES

(1) Wang, Y.; Li, X.; Song, J.; Xiao, L.; Zeng, H.; Sun, H. All-Inorganic Colloidal Perovskite Quantum Dots: A New Class of Lasing Materials with Favorable Characteristics. *Adv. Mater.* **2015**, *27*, 7101−7108.

(2) Song, J.; Li, J.; Li, X.; Xu, L.; Dong, Y.; Zeng, H. Quantum Dot Light-Emitting Diodes Based on Inorganic Perovskite Cesium Lead Halides ($CsPbX_3$). *Adv. Mater.* **2015**, *27*, 7162−7167.

(3) Protesescu, L.; Yakunin, S.; Bodnarchuk, M. I.; Krieg, F.; Caputo, R.; Hendon, C. H.; Yang, R. X.; Walsh, A.; Kovalenko, M. V. Nanocrystals of Cesium Lead Halide Perovskites ($CsPbX_3$, X = Cl, Br, and I): Novel Optoelectronic Materials Showing Bright Emission with Wide Color Gamut. *Nano Lett.* **2015**, *15*, 3692−3696.

(4) Swarnkar, A.; Chulliyil, R.; Ravi, V. K.; Irfanullah, M.; Chowdhury, A.; Nag, A. Colloidal $CsPbBr_3$ Perovskite Nanocrystals: Luminescence beyond Traditional Quantum Dots. *Angew. Chem., Int. Ed.* **2015**, *54*, 15424−15428.

(5) Xiang, X.; Lin, H.; Li, R.; Cheng, Y.; Huang, Q.; Xu, J.; Wang, C.; Chen, X.; Wang, Y. Stress-Induced $CsPbBr_3$ Nanocrystallization on Glass Surface: Unexpected Mechanoluminescence and Applications. *Nano Res.* **2019**, *12*, 1049−1054.

(6) Yang, D.; Li, X.; Zhou, W.; Zhang, S.; Meng, C.; Wu, Y.; Wang, Y.; Zeng, H. $CsPbBr_3$ Quantum Dots 2.0: Benzenesulfonic Acid Equivalent Ligand Awakens Complete Purification. *Adv. Mater.* **2019**, *31*, No. 1900767.

(7) Li, X.; Wu, Y.; Zhang, S.; Cai, B.; Gu, Y.; Song, J.; Zeng, H. $CsPbX_3$ Quantum Dots for Lighting and Displays: Room-Temperature Synthesis, Photoluminescence Superiorities, Underlying Origins and White Light-Emitting Diodes. *Adv. Funct. Mater.* **2016**, *26*, 2435−2445.

(8) Kovalenko, M. V.; Protesescu, L. M.; Bodnarchuk, I. Properties and Potential Optoelectronic Applications of Lead Halide Perovskite Nanocrystals. *Science* **2017**, *358*, 745−750.

(9) Lin, K.; Xing, J.; Quan, L. N.; de Arquer, F. P. G.; Gong, X.; Lu, J.; Xie, L.; Zhao, W.; Zhang, D.; Yan, C.; et al. Perovskite Light-Emitting Diodes with External Quantum Efficiency Exceeding 20 per Cent. *Nature* **2018**, *562*, 245−248.

(10) Wei, Y.; Cheng, Z.; Lin, J. An Overview on Enhancing the Stability of Lead Halide Perovskite Quantum Dots and Their Applications in Phosphor-Converted LEDs. *Chem. Soc. Rev.* **2019**, *48*, 310−350.

(11) Wang, H. C.; Lin, S. Y.; Tang, A. C.; Singh, B. P.; Tong, H. C.; Chen, C. Y.; Lee, Y. C.; Tsai, T. L.; Liu, R. S. Mesoporous Silica Particles Integrated with All-Inorganic $CsPbBr_3$ Perovskite Quantum-Dot Nanocomposites (MP-PNCs) with High Stability and Wide Color Gamut Used for Backlight Display. *Angew. Chem., Int. Ed.* **2016**, *55*, 7924−7929.

(12) Li, Z.; Kong, L.; Huang, S.; Li, L. Highly Luminescent and Ultrastable $CsPbBr_3$ Perovskite Quantum Dots Incorporated into a Silica/Alumina Monolith. *Angew. Chem., Int. Ed.* **2017**, *56*, 8134−8138.

(13) Sun, C.; Zhang, Y.; Ruan, C.; Yin, C. Y.; Wang, X. Y.; Wang, Y. D.; Yu, W. W. Efficient and Stable White LEDs with Silica-Coated Inorganic Perovskite Quantum Dots. *Adv. Mater.* **2016**, *28*, 10088−10094.

(14) Bertolotti, F.; Protesescu, L.; Kovalenko, M. V.; Yakunin, S.; Cervellino, A.; Billinge, S. J. L.; Terban, M. W.; Pedersen, J. S.; Masciocchi, N.; Guagliardi, A. Coherent Nanotwins and Dynamic Disorder in Cesium Lead Halide Perovskite Nanocrystals. *ACS Nano* **2017**, *11*, 3819−3831.

(15) Deutsch, Z.; Neeman, L.; Oron, D. Luminescence Upconversion in Colloidal Double Quantum Dots. *Nat. Nanotechnol.* **2013**, *8*, 649−653.

(16) Pan, J.; Sarmah, S. P.; Murali, B.; Dursun, I.; Peng, W.; Parida, M. R.; Liu, J.; Sinatra, L.; Alyami, N.; Zhao, C.; Alarousu, E.; Ng, T. K.; Ooi, B. S.; Bakr, O. M.; Mohammed, O. F. Air-Stable Surface-Passivated Perovskite Quantum Dots for Ultra-Robust, Single- and Two-Photon-Induced Amplified Spontaneous Emission. *J. Phys. Chem. Lett.* **2015**, *6*, 5027−5033.

(17) Wang, Y.; Li, X.; Zhao, X.; Xiao, L.; Zeng, H.; Sun, H. Nonlinear Absorption and Low-Threshold Multiphoton Pumped Stimulated Emission from All-Inorganic Perovskite Nanocrystals. *Nano Lett.* **2016**, *16*, 448−453.

(18) Xu, Y.; Chen, Q.; Zhang, C.; Wang, R.; Wu, H.; Zhang, X.; Xing, G.; Yu, W. W.; Wang, X.; Zhang, Y.; Xiao, M. Two-Photon-Pumped Perovskite Semiconductor Nanocrystal Lasers. *J. Am. Chem. Soc.* **2016**, *138*, 3761−3768.

(19) Chen, J.; Žídek, K.; Chabera, P.; Liu, D.; Cheng, P.; Nuuttila, L.; Al-marri, M. J.; Lehtivuori, H.; Messing, M. E.; Han, K.; et al. Size and Wavelength Dependent Two-Photon Absorption Cross-Section of $CsPbBr_3$ Perovskite Quantum Dots. *J. Phys. Chem. Lett.* **2017**, *8*, 2316−2321.

(20) Wang, F.; Liu, X. G. Recent Advances in the Chemistry of Lanthanide-Doped Upconversion Nanocrystals. *Chem. Soc. Rev.* **2009**, *38*, 976−989.

(21) Yang, D.; Ma, P.; Hou, Z.; Cheng, Z.; Li, C.; Lin, J. Current Advances in Lanthanide Ion (Ln^{3+})-Based Upconversion Nanomaterials for Drug Delivery. *Chem. Soc. Rev.* **2015**, *44*, 1416−1448.

(22) Zhou, B.; Shi, B. Y.; Jin, D. Y.; Liu, X. G. Controlling Upconversion Nanocrystals for Emerging Applications. *Nat. Nanotechnol.* **2015**, *10*, 924−936.

(23) Zhou, B.; Yan, L.; Tao, L. L.; Song, N.; Wu, M.; Wang, T.; Zhang, Q. Y. Enabling Photon Upconversion and Precise Control of

Donor-Acceptor Interaction through Interfacial Energy Transfer. *Adv. Sci.* **2018**, *5*, No. 1700667.
(24) Zheng, W.; Huang, P.; Gong, Z.; Tu, D.; Xu, J.; Zou, Q.; Li, R.; You, W.; Bünzli, J. C. G.; Chen, X. Near-Infrared-Triggered Photon Upconversion Tuning in All-Inorganic Cesium Lead Halide Perovskite Quantum Dots. *Nat. Commun.* **2018**, *9*, No. 3262.
(25) Yuan, S.; Chen, D.; Li, X.; Zhong, J.; Xu, X. In Situ Crystallization Synthesis of $CsPbBr_3$ Perovskite Quantum Dot-Embedded Glasses with Improved Stability for Solid-State Lighting and Random Upconverted Lasing. *ACS Appl. Mater. Interfaces* **2018**, *10*, 18918−18926.
(26) Chen, D.; Yuan, S.; Chen, J.; Zhong, J.; Xu, X. Robust $CsPbX_3$ (X = Cl, Br, and I) Perovskite Quantum Dot Embedded Glasses: Nanocrystallization, Improved Stability and Visible Full-Spectral Tunable Emissions. *J. Mater. Chem. C* **2018**, *6*, 12864−12870.
(27) Ye, Y.; Zhang, W.; Zhao, Z.; Wang, J.; Liu, C.; Deng, Z.; Zhao, X.; Han, J. Highly Luminescent Cesium Lead Halide Perovskite Nanocrystals Stabilized in Glasses for Light-Emitting Applications. *Adv. Opt. Mater.* **2019**, *7*, No. 1801663.
(28) Xia, M.; Luo, J.; Chen, C.; Liu, H.; Tang, J. Semiconductor Quantum Dots-Embedded Inorganic Glasses: Fabrication, Luminescent Properties, and Potential Applications. *Adv. Opt. Mater.* **2019**, *7*, No. 1900851.
(29) Ai, B.; Liu, C.; Wang, J.; Xie, J.; Han, J.; Zhao, X.; Heo, J. Precipitation and Optical Properties of $CsPbBr_3$ Quantum Dots in Phosphate Glasses. *J. Am. Ceram. Soc.* **2016**, *99*, 2875−2877.
(30) Cheng, Y.; Shen, C.; Shen, L.; Xiang, W.; Liang, X. Tb^{3+}, Eu^{3+} Co-Doped $CsPbBr_3$ QDs Glass with Highly Stable and Luminous Adjustable for White LEDs. *ACS Appl. Mater. Interfaces* **2018**, *10*, 21434−21444.
(31) Chen, D.; Liu, Y.; Yang, C.; Zhong, J.; Zhou, S.; Chen, J.; Huang, H. Promoting Photoluminescence Quantum Yields of Glass-Stabilized $CsPbX_3$ (X = Cl, Br, I) Perovskite Quantum Dots through Fluorine Doping. *Nanoscale* **2019**, *11*, 17216−17221.
(32) Zhou, D.; Liu, D.; Pan, G.; Chen, X.; Li, D.; Xu, W.; Bai, X.; Song, H. Cerium and Ytterbium Codoped Halide Perovskite Quantum Dots: A Novel and Efficient Downconverter for Improving the Performance of Silicon Solar Cells. *Adv. Mater.* **2017**, *29*, No. 1704149.
(33) Mir, W. J.; Sheikh, T.; Arfin, H.; Xia, Z.; Nag, A. Lanthanide Doping in Metal Halide Perovskite Nanocrystals: Spectral Shifting, Quantum Cutting and Optoelectronic Applications. *NPG Asia Mater.* **2020**, *12*, 9.
(34) Chen, N.; Cai, T.; Li, W.; Kimball, K.; Yang, H.; Que, M.; Nagaoka, Y.; Liu, Z.; Yang, D.; Dong, A.; Xu, C.; Zia, R.; Chen, O. Yb- and Mn-Doped Lead-Free Double Perovskite Cs_2AgBiX_6 ($X = Cl^-$, Br^-) Nanocrystals. *ACS Appl. Mater. Interfaces* **2019**, *11*, 16855−16863.
(35) Arfin, H.; Kaur, J.; Sheikh, T.; Chakraborty, S.; Nag, A. Bi^{3+}-Ln^{3+} (Ln = Er and Yb) codoped $Cs_2AgInCl_6$ Double Perovskite Near Infrared Emitter. *Angew. Chem., Int. Ed.* **2020**, DOI: 10.1002/anie.202002721.
(36) Chen, D.; Liu, S.; Wan, Z.; Chen, Y. A Highly Sensitive Upconverting Nano-Glass-Ceramic-Based Optical Thermometer. *J. Alloys Compd.* **2016**, *672*, 380−385.
(37) Xu, W.; Zhang, Z.; Cao, W. Excellent Optical Thermometry Based on Short-Wavelength Upconversion Emissions in Er^{3+}/Yb^{3+} Co-doped $CaWO_4$. *Opt. Lett.* **2012**, *37*, 4865.
(38) Tu, X.; Xu, J.; Li, M.; Xie, T.; Lei, R.; Wang, H.; Xu, S. Color-Tunable Upconversion Luminescence and Temperature Sensing Behavior of Tm^{3+}/Yb^{3+} Codoped $Y_2Ti_2O_7$ Phosphors. *Mater. Res. Bull.* **2019**, *112*, 77−83.
(39) Song, H.; Wang, C.; Han, Q.; Tang, X.; Yan, W.; Chen, Y.; Jiang, J.; Liu, T. Highly Sensitive Tm^{3+} /Yb^{3+} Codoped $SrWO_4$ for Optical Thermometry. *Sens. Actuators, A* **2018**, *271*, 278−282.
(40) Liu, S.; Cui, J.; Jia, J.; Fu, J.; You, W.; Zeng, Q.; Yang, Y.; Ye, X. High Sensitive $Ln^{3+}/Tm^{3+}/Yb^{3+}$ (Ln^{3+} = Ho^{3+}, Er^{3+}) Tri-Doped $Ba_3Y_4O_9$ Upconverting Optical Thermometric Materials Based on Diverse Thermal Response from Non-Thermally Coupled Energy Levels. *Ceram. Int.* **2019**, *45*, 1−10.
(41) Zhang, H.; Gao, Z.; Li, G.; Zhu, Y.; Liu, S.; Li, K.; Liang, Y. A Ratiometric Optical Thermometer with Multi-Color Emission and High Sensitivity Based on Double Perovskite $LaMg_{0.402}Nb_{0.598}O_3$: Pr^{3+} Thermochromic Phosphors. *Chem. Eng. J.* **2020**, *380*, No. 122491.
(42) Zhu, Z.; Sun, Z.; Guo, Z.; Zhang, X.; Wu, Z. C. A High-Sensitive Ratiometric Luminescent Thermometer Based on Dual-Emission of Carbon Dots/Rhodamine B Nanocomposite. *J. Colloid Interface Sci.* **2019**, *552*, 572−582.

https://dx.doi.org/10.1021/acsami.0c01968
ACS Appl. Mater. Interfaces 2020, 12, 18705−18714